2−1

High Enthalpy Air Flow Computations with a Sphere and a Blunted Cone Models

Igor MEN'SHOV and Yoshiaki NAKAMURA

Dep. of Aerospace Engineering, Nagoya University

ABSTRACT

A computational fluid dynamics (CFD) technique is employed to study hypersonic high enthalpy air flow around blunt bodies at a range of enthalpies relevant to suborbital flight speeds of aeroassisted orbital transfer vehicles (ASTVs). The method uses the two-temperature model of Park for the description of thermo-chemical nonequilibrium processes in high temperature air and solves the full Navier-Stokes equations for multicomponent reacting gas mixture in finite volume formulation on a grid of arbitrary structure. The calculations performed in this work simulate in detail the experiments carried out recently at the KHI (Japan), and at the DLR (Germany), where heat flux distribution over a sphere and a capsule-like blunt cone model was measured at several freestream conditions related to the range of enthalpies mentioned above. The main emphasis in this paper is given to comparison between numerical and experimental results in order to verify adequacy of data in terms of heat flux distributions predicted by the CFD technique for suborbital ASTV flight range.

1. Introduction

The assessment of heating load during re-entry has always been one of key points in the design of ASTVs. This problem has been extensively investigated initially by both experimental and analytical methods for the purpose of estimating the convective heat transfer rates at the stagnation point (e.g. Refs.1, and 2). However, all these experiments and theoretical considerations were performed at the range too far from flight situations that may be encountered by ASTVs, and where nonequilibrium phenomena are not essential and the flow can be considered on the assumption of thermo-chemical equilibrium.

The development of experimental base makes now possible to realize high enthalpy flow experiments through a range of enthalpies: 2.5 MJ/kg to 45 MJ/kg, equivalent to velocities: 2 km/s to 10 km/s, which covers re-entry flight speeds of the ASTV (e.g. Refs.3, and 4), and where nonequilibrium effects should play a considerable role. The results derived from these experiments are of crucial importance for the justification of existing CFD's models for flows in chemical and thermal nonequilibrium mainly in the question that to what extent these models can predict close to real values such basic thermo- and aerodynamic characteristics as forces, moments, and heat flux rates.

The two-temperature model of Park (Ref.5) seems at present to be a most widely used model in the CFD for the simulation of high enthalpy nonequilibrium air flows. In this model, two assumptions are made to describe species' energy distributions. The first is that the translational mode is in equilibrium with the rotational mode and the distribution of energies in these two modes are described by one translational-rotational temperature for all heavy particle species. In the second one, another temperature (vibrational-electronic) is introduced to characterize the vibrational energy of molecules, translational energy of electrons, and electronic excitation energy of atoms and molecules.

Supported by many experimental data, a justification for the two-temperature model is based on the facts that (a) the energy transfer between the translational and rotational modes, and between the translational mode of free electrons and the vibrational mode of molecular nitrogen are very fast, and (b) the low-level electronic states of heavy particles become equilibrium very quickly with the ground electronic state at the electronic temperature.

In Ref. 6, the effects of thermochemical nonequilibrium on forces and moments at hypersonic flight speeds were studied by using Park's model, and a 10% change in lift and drag and a 20% change in pitching moment for the airfoil caused by the nonequilibrium phenomena were numerically predicted. In this paper, we make an attempt to apply the two-temperature model in the prediction of heat characteristics by numerically simulating the experiments carried recently out at the DLR, Germany (Ref.3), and at the KHI, Japan (Ref. 4), where convective heat flux distribution over model' surface was measured at different freestream conditions with enthalpies ranging from 20 MJ/kg to 40 MJ/kg.

Towards this end, a numerical code for obtaining steady-state solutions to the equations of 2D fluid motion coupled with the finite-rate chemistry in thermal and chemical nonequilibrium air has been developed in the Fluid Dynamics Laboratory, Department of Aerospace Engineering, Nagoya University. The code basically described in Ref.7 solves the Euler or Navier-Stokes equations for multicomponent reacting gas flow in finite-volume formulation on a grid of arbitrary structure. Inviscid convective terms are discretized with a modification of the Advection Upstream Splitting Method (AUSM) (Ref. 8). Viscous fluxes are approximated with a standard centered scheme. Time integration is performed in two-step implicit manner, and an approximate linearization is made for inviscid and viscous fluxes and exact that is used for the thermo-chemical sources. The approximate linearization of the

inviscid fluxes is performed based on the method proposed in Ref. 9, which leads to an implicit operator in diagonal form after applying the Lower Upper Symmetric Gauss-Siedel (LU-SGS) factorization (Ref. 9) in the case of strucured grid. We proved that this remarkable property is conserved if the LU-SGS factorization is applied to unstructured grid, and hence independently on the grid considered, in order to invert the implicit operator in this way only the Jacobian matrix of the thermochemical source needs to be inverted in each computational cell.

2. Physical model and governing equations

With the exception of ionization phenomena that are neglected in this paper, we closely follow the two-temperature model of Park (Ref.10). The five neutral species: N, O, NO, N_2, O_2 are considered and 17 most important chemical reactions among these species are employed. The reaction rate coefficients are controlled by the temperature (rate-controlling temperature), which is a geometrically averaged temperature between the translational-rotational and vibrational-electronic temperatures. The rate parameters are cited from Ref. 11.

Transport coefficients are evaluated by extending Yos's formula based on the first Chapman-Enskog approximation to multitemperature gas mixture (Ref.12). To simplify evaluation of the collision integrals in Yos's formula, the formulas of Chapman and Cowling for species viscosity and binary-diffusion coefficient along with the semiempirical formula of Wilke for mixture viscosity (Ref.13) are invoked. Comparing these formulas with the corresponding Yos's ones, compact and easily computed expressions can be obtained for the collision integrals by which the transport coefficients are expressed.

The relaxation of vibrational-electronic excitation energy due to collisions with heavy particles is modeled according to the theory of Landau and Teller (Ref.14). The relaxation time employed in this theory is computed as the sum of the empirical correlations of Millikan and White and high temperature correction proposed by Park (Ref. 15).

The system of governing equations with the physical model described above can be expressed as follows:

$$\partial_t \mathbf{q} + \partial_k \mathbf{f}_k = \partial_k \mathbf{g}_k + \mathbf{H} \qquad (1)$$

where $\mathbf{q}$ is the solution vector, the components of which are the species densities, 3 momentum components, the vibrational-electronic excitation energy, and the total energy, respectively. The vectors $\mathbf{f}_k$ and $\mathbf{g}_k$ $(k = 1,2,3)$ are inviscid and viscous flux vectors, respectively, and $\mathbf{H}$ is the thermochemical source. The summation on repeating index is assumed in eq.(1) and hereafter.

3. Numerical algorithm

We use the finite volume method with two-step implicit time integration to obtain spatial and time discretizations of the governing equations (1) . Having been given a spatial decomposition, which is structured or unstructered, of the computational domain by a set of control volumes (CV), the resulting system of discrete equations can be written as:

$$\omega_i \Delta \mathbf{q}_i + \Delta t \sum_\sigma s_\sigma \mathbf{f}_\sigma^{n+1} = \Delta t \sum_\sigma s_\sigma \mathbf{g}_\sigma^{n+1} + \omega_i \Delta t \mathbf{H}_i^{n+1}, \qquad (2)$$

$$\mathbf{f}_\sigma = \mathbf{f}_{k,\sigma} n_k, \quad \mathbf{g}_\sigma = \mathbf{g}_{k,\sigma} n_k, \quad i = 1,\ldots,N$$

where $\mathbf{q}_i$ is the solution vector averaged on the CV, ω_i is the CV volume, s_σ is the area of the CV interface, $\mathbf{n} = (n_1, n_2, n_3)$ is the exterior normal to the CV interface. Here the superscript denotes the time level, σ denotes the CV interface, and Δ denotes the increment in time. The summation in eq. (2) is performed for all faces bordering the CV under consideration.

The inviscid numerical flux $\mathbf{f}_\sigma$ at the interface σ is expressed in terms of the local one-dimensional flux $\mathbf{F}$ as follows:

$$\mathbf{f}_\sigma = \mathbf{T}_\sigma^{-1} \mathbf{F}, \quad \mathbf{F} = \mathbf{f}_1(\mathbf{Q}), \quad \mathbf{Q} = \mathbf{T}_\sigma \mathbf{q} \qquad (3)$$

where $\mathbf{T}_\sigma$ is the transforming matrix defined by the coordinates of the unit vectors of the local orthonormal basis at the interface (Ref.16).

To solve the system of discrete equations (2) we linearize the thermochemical source vector and approximate the inviscid local flux and the viscous flux in the following way (Refs.7, and 17):

$$\mathbf{F}^{n+1} = \mathbf{F}^n + \mathbf{A}_i^+ \Delta \mathbf{Q}_i + \mathbf{A}_{\sigma(i)}^- \Delta \mathbf{Q}_{\sigma(i)} \qquad (4)$$

$$\mathbf{g}_\sigma^{n+1} = \mathbf{g}_\sigma^n + \mathbf{D}_\sigma (\Delta \mathbf{q}_{\sigma(i)} - \Delta \mathbf{q}_i)$$

Here, $\mathbf{A}^+$ is a positive matrix, and $\mathbf{A}^-$ is a negative matrix such that their sum equals to the Jacobian matrix of the flux $\mathbf{F}$ with respect to the vector $\mathbf{Q}$:

$$\mathbf{A}^+ + \mathbf{A}^- = \mathbf{A} = \partial \mathbf{F} / \partial \mathbf{Q} \qquad (5)$$

The coefficient D_σ in eq. (4) is taken in the form:

$$D_\sigma = \rho_{dis} / h_\sigma \qquad (6)$$

$$\rho_{dis} = \max(d_1, \ldots, d_5, \nu, \alpha, \alpha_v)$$

where d_k $(k = 1$ to $5)$ are diffusion coefficients, ν is the viscous diffusivity, α, α_v are the thermal diffusivity for translational-rotational and vibrational-electronic mode, respectively, and h_σ is the distance between i- and $\sigma(i)$-node points projected on the normal to the interface, $h_\sigma = |\mathbf{n} \bullet (\mathbf{x}_i - \mathbf{x}_{\sigma(i)})|$.

By substituting eq. (4) in eq. (2), we obtain the system of linear equations with respect to the increment of the solution vector:

$$(\mathbf{I} + \sum_\sigma \mu_i^+ - \Delta t \mathbf{S}_i) \Delta \mathbf{q}_i + \sum_\sigma \mu_{\sigma(i)}^- \Delta \mathbf{q}_{\sigma(i)} = \mathbf{R}_i \qquad (7)$$

where $\mathbf{S}_i$ is the Jacobian matrix of the thermochemical source vector $\mathbf{H}_i$. $\mathbf{R}_i$ is the residual defined as

$$\mathbf{R}_i = \Delta t \mathbf{H}_i^n + \frac{\Delta t}{\omega_i} \sum_\sigma s_\sigma (\mathbf{g}_\sigma^n - \mathbf{f}_\sigma^n) \qquad (8)$$

and the matrices $\mu^\pm$ are defined at each CV interface as follows:

$$\mu^\pm = \frac{\Delta t}{\omega_i} s_\sigma (\mathbf{T}_\sigma^{-1} \mathbf{A}^\pm \mathbf{T}_\sigma \pm D_\sigma \mathbf{I}) \qquad (9)$$

The system of equations (7) has a large block band matrix, which requires many operations for its

inversion. To reduce the computational cost, which is usually encountered in direct solvers, the matrix in the left hand side of eq. (7) is often approximately factorized as product of a number of easily invertible factors. One of such factorizations referred to as the Lower-Upper Symmetric Gauss-Siedel (LU-SGS) method was proposed in Ref. 9 for strucured spatial discretizations. We employ this method and extend it to unstructured grids to solve eq. (7).

The generalization of the LU-SGS to unstructured grids is obtained in the following way (see Ref.16). First, the second term in the left hand side of eq. (7) is represented by the sum of two terms:

$$\sum_{\sigma} \mu^{-}_{\sigma(i)} \Delta \mathbf{q}_{\sigma(i)} = \Sigma_L(\Delta \mathbf{q}) + \Sigma_U(\Delta \mathbf{q}) \qquad (10)$$

where

$$\Sigma_L(\Delta \mathbf{q}) = \sum_{\sigma:\sigma(i)<i} \mu^{-}_{\sigma(i)} \Delta \mathbf{q}_{\sigma(i)} \qquad (11)$$

$$\Sigma_U(\Delta \mathbf{q}) = \sum_{\sigma:\sigma(i)>i} \mu^{-}_{\sigma(i)} \Delta \mathbf{q}_{\sigma(i)}$$

Then, the equation (7) is replaced by the two coupled equations

$$(I + \sum_{\sigma} \mu^{+}_{i} - \Delta t S_i) \Delta \mathbf{q}^{*}_{i} = -\Sigma_L(\Delta \mathbf{q}^{*}) + \mathbf{R}_i \qquad (12.1)$$

$$(I + \sum_{\sigma} \mu^{+}_{i}) \Delta \mathbf{q}_{i} = -\Sigma_U(\Delta \mathbf{q}) + (I + \sum_{\sigma} \mu^{+}_{i}) \Delta \mathbf{q}^{*}_{i} \qquad (12.2)$$

which are used for calculating intermediate values of the increment, $\Delta \mathbf{q}^{*}_{i}$, and its final values, $\Delta \mathbf{q}_{i}$, respectively.

The system (12.1) has a lower triangular matrix, while that of (12.2) is a upper triangular with elements of block (Nsp+5)×(Nsp+5) matrices, where Nsp is the number of species. It allows us to efficiently solve eqs. (12.1) and (12.2) by implementing forward (i=1,...,N) and backward (i=N,...,1) relaxation sweeps, which involve the inversion of the block (Nsp+5)×(Nsp+5) matrices on the diagonal only. Thus, the final increment $\Delta \mathbf{q}_i$ can be obtained, which then used to update the solution vector $\mathbf{q}_i$.

The method described above needs to be comleted by setting up the formulas for the approximation of inviscid and viscous fluxes at the lower time level, and by defining concretely the Jacobian matrix splitted in eq. (5).

The discretization of the viscous terms requires an approximation to the derivatives of the solution vector at each face of the CV. In order to evaluate the derivatives we employ the following two-step procedure. First, the solution vector is interpolated from cell centers to cell vertices. Then, the derivatives are calculated by applying the Gauss formula to a dual cell coupled with the face.

To approximate the inviscid flux, a modification to the Advection Upstream Splitting Method (AUSM) proposed in Ref. 8 is used. A key issue of the AUSM is to divide the flux vector **F** into two terms: convective and pressure terms, and approximate them separately. The main achievement of this approach is that a stationary contact discontinuity can be captured without excess numerical dissipation, and consequently, shear layers can be calculated quite accurately even with a first order approximation.

Introducing the vector Φ with the components

$$\Phi_k = Q_k, \quad k \neq Nsp+5 \qquad (13)$$

$$\Phi_{Nsp+5} = Q_{Nsp+5} + p$$

the flux vector **F** can be expressed as

$$\mathbf{F} = u\Phi + \mathbf{P} \qquad (14)$$

where u is the projection of the velocity vector onto the exterior normal to the interface, and the pressure term **P** has the following components

$$P_k = 0, \quad k \neq Nsp+1 \qquad (15)$$

$$P_{Nsp+1} = p$$

Here p denotes the pressure.

The first term on the right hand side of eq. (14) can be treated as a passive advection of the vector Φ with the velocity u, and approximated in upwind fashion according to a suitable defined velocity u_σ. Approximation of the pressure term is in fact to define an appropriate value for the pressure at the interface p_σ. In this way, giving values to interface pressure and velocity, one can obtain a two-parametric approximation to the inviscid flux **F**, which can be written in the following form:

$$\mathbf{F} = 0.5\left[u_\sigma(\Phi_i + \Phi_{\sigma(i)}) - |u_\sigma|(\Phi_{\sigma(i)} - \Phi_i)\right] + \mathbf{P}_\sigma \qquad (16)$$

Hence, a specific approximation to the flux **F** is uniquely defined by an appropriate interface velocity u_σ and an interface pressure p_σ. In the AUSM scheme, these values are defined with Van Leer's splitting procedure (Ref.18) as

$$u_\sigma = u^{+}_{i} + u^{-}_{\sigma(i)} \qquad (17)$$

$$p_\sigma = p^{+}_{i} + p^{-}_{\sigma(i)}$$

where

$$u^{\pm} = \begin{cases} \pm 0.25a(M \pm 1)^2, & \text{if } |M| \le 1 \\ 0.5a(M \pm |M|), & \text{otherwise} \end{cases} \qquad (18)$$

$$p^{\pm} = \begin{cases} 0.25p(M \pm 1)^2(2 \mp M), & \text{if } |M| \le 1 \\ 0.5p(M \pm |M|)/M, & \text{otherwise} \end{cases}$$

Here a is the sound velocity, and M=u/a is the Mach number.

The definition of the inviscid flux as eqs. (16) to (18) is computationaly very simple, and requires *O*(Nsp+5) operations per grid point. At the same time, numerous numerical experiments show that it provides just the same accuracy in capturing discontinuities as Godunov's type schemes based on the solution of the local Riemann problem. In addition to these positive properties, the method has the disadvantage that it may produce slight numerical overshoots just behind shock waves, essentialy precluding the possibility of an accurate high-order extension in the vicinity of shock waves.

In Ref.19, the reason of these overshoots is supposed to be due to the fact that the mass flux in (16) does not directly take into account of the density behind the shock wave. Several attempts have been performed to eliminate these overshoots (Refs.19, and 20), based

mostly on the adding of blending elements of more diffusive schemes into the AUSM formulation. In this paper, we propose a very simple modification to the AUSM, which alleviates the monotonicity problems.

In authors' opinion, the nonmonotonicity at shocks might be caused by the definition of the interface velocity in the form of Van Leer's splitting. In fact, because the first term in eq. (16) is treated as a passive advection of the vector Φ, the propagation of disturbances in this process is defined by one eigenvalue of the Jacobian matrix A, which is equal to the normal velocity u, while the pressure disturbance propagation is in accordance with two acoustic eigenvalues. Therefore, the evaluation of p_σ in a splitting manner is justified, but as for u_σ , an interpolation between u_i and $u_{\sigma(i)}$ seems to be a more plausible approach.

To this end, we substitute the splitting form definition of u_σ in (17), and (18) by the symmetric averaging:

$$u_\sigma = 0.5(u_i + u_{\sigma(i)}) \tag{19}$$

It was observed in numerous numerical experiments that due to this modification the overshoots can be eliminated, and the method produce monotonic solution behind shock waves. As an example, Figure 1 illustrates the density contours for hypersonic flow around a cylinder at the freestream Mach number of 20 computed assuming non-reacting inviscid perfect gas by the AUSM with formulas (17), and (18) (Fig.1a), and (19) (Fig.1b) for the interface velocity u_σ on a coarse grid of 15x40 meshes.

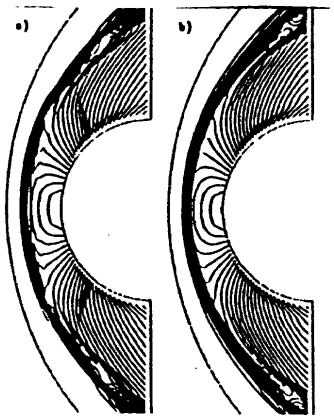

Fig.1 Density contours: a) splitting, b) averaging velocity

The system of discrete equations (12.1), and (12.2) can be written in the standart LU operator form as follows:

$$LD^{-1}U\Delta q = R \tag{21}$$

where

$$L = D + \Sigma_L - \Delta t S, \quad U = D + \Sigma_U \tag{22}$$

$$D = \tilde{D} + (1 + \frac{\Delta t}{\omega}\sum_\sigma D_\sigma)I, \quad \tilde{D} = \frac{\Delta t}{\omega}\sum_\sigma s_\sigma T_\sigma^{-1} A^+ T_\sigma$$

If the thermochemical noneqilibrium process are not considered (S=0), then the solution to eq. (21) requires inversion of the operator D only. A merit of the LU-SGS approximate factorization is found when it is used coupled with the Jacobian matrix splitting proposed in Ref. 22:

$$A^\pm = 0.5(A \pm \rho_A) \tag{23}$$

If a structured grid is used and a transformation to curvilinear coordinates followed by the LU-SGS factorization with the splitting (23) is performed, the operator D in eq. (21) is reduced to a diagonal form, and any matrix inversion is excluded from the algorithm (Ref.9).

It appears that this remarkable property is kept even in a general approach described above. This fact comes from the following property of the Jacobian matrix A, which is formulated for simliticity for a non-reacting one-component gas model in the following

Lemma. Let S be a closed surface in R^3, $\mathbf{n}=(n_1,n_2,n_3)$, $\mathbf{k}=(k_1,k_2,k_3)$, $\mathbf{l}=(l_1,l_2,l_3)$ are unit vectors of the orthonormal basis at S, where $\mathbf{n}$ is the exterior normal, and $\mathbf{k}$, $\mathbf{l}$ are tangential unit vectors to S. T_s is the transforming matrix associated with the basis:

$$T_s = \begin{vmatrix} 1 & 0 & 0 & 0 & 0 \\ 0 & n_1 & n_2 & n_3 & 0 \\ 0 & k_1 & k_2 & k_3 & 0 \\ 0 & l_1 & l_2 & l_3 & 0 \\ 0 & 0 & 0 & 0 & 1 \end{vmatrix} \tag{24}$$

$\mathbf{q}$ is the conservative solution vector, $\mathbf{Q}=T_s\mathbf{q}$, and $\mathbf{F}=\mathbf{F}(\mathbf{Q})$ is the local one-dimensinal inviscid flux associated with the basis.

Then, for any constant vector $\mathbf{q}$ the Jacobian matrix $A=\partial F/\partial Q$ satisfies the following identity:

$$\int_s T_s^{-1} A T_s ds \equiv 0 \tag{25}$$

Proof. The identity (25) comes from the conservative property of the inviscid flux:

$$\int_s f_m n_m ds \equiv 0 \tag{26}$$

From eq. (3) we can rewrite this as

$$\int_s T_s^{-1} F ds \equiv 0 \tag{27}$$

As $\mathbf{F}$ is the homogeneous function of degree one in $\mathbf{Q}$, one can substitute $\mathbf{F} = AQ = AT_s\mathbf{q}$ and obtain

$$\int_s T_s^{-1} A T_s \mathbf{q} ds \equiv 0 \tag{28}$$

from which (25) follows immediately.

It follows from the lemma that the matrix $\tilde{D}$ in (22) with the splitting (23) reduces to the diagonal matrix

$$\tilde{D} = 0.5\frac{\Delta t}{\omega}\sum_\sigma \rho_A I \tag{29}$$

for an arbitrary unstructured spatial discretization, and any matrix inversion is not required to solve the discrete equation (21) if S=0. For reacting gas flow, the Jacobian matrix of thermochemical source, S, needs to be inverted at each computational cell only.

3. Sphere model calculations

Calculations are performed for the flow around a sphere to simulate the experiments carried out at the K.H.I. (Ref.4). The radius of the sphere r_{sp} is 2cm. In these experiments, the heat transfer rate along the

sphere surface was measured for three cases of freestream conditions listed in Table I.

Table I

Case	A	B	C
V_∞, km/s	5.939	6.180	5.151
ρ_∞, kg/m^3	0.00156	0.0034	0.0058
T_∞, K	705	934	708
m.frac., N	0	0	0
m.frac., O	0.1708	0.1468	0.0406
m.frac., NO	0.0317	0.0429	0.0688
m.frac., N_2	0.762	0.744	0.733
m.frac., O_2	0.0348	0.0659	0.1578
M_∞	10.19	9.33	9.43
Re_∞	33535.6	64148.3	120641

A nonuniform grid consisting of 60 cells in the radial direction and 30 (60 in the case C) cells in the direction along the sphere surface is clustered in the boundary layer and characterized by a minimum cell size at the sphere wall, h_{min}, which is taken such that the cell Reynolds number at the wall varies from 1 to 3 depending on the calculations.

The total heat flux q_h is calculated by the summation of 3 contribution parts: translational temperature mode flux, vibrational temperature mode flux, and diffusion mode flux:

$$q_h = k\frac{\partial T}{\partial n} + k_v\frac{\partial T_v}{\partial n} + \rho\sum_{s=1}^{5} h_s D_s \frac{\partial Y_s}{\partial n} \qquad (30)$$

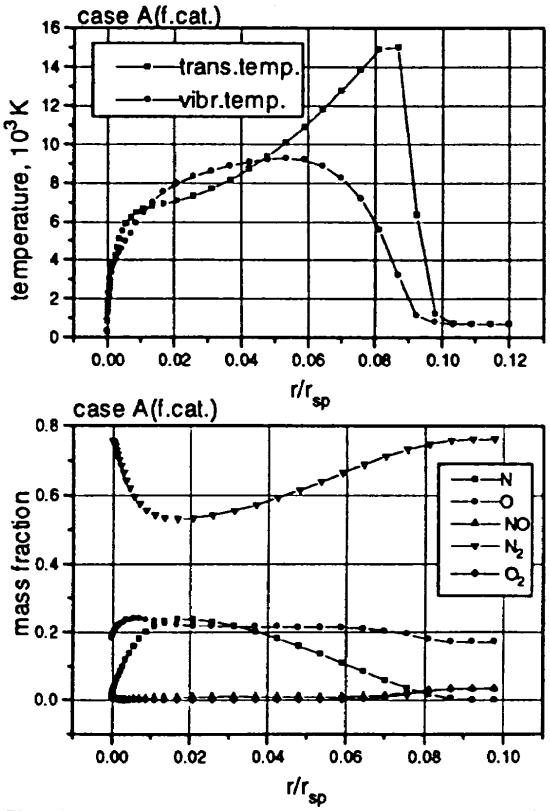

Fig.2 Case A: mass fraction and temperature along stagnation line

Both fully catalytic and non-catalytic boundary conditions are imposed at the wall, the temperature of which is assumed to be 300K for all cases.

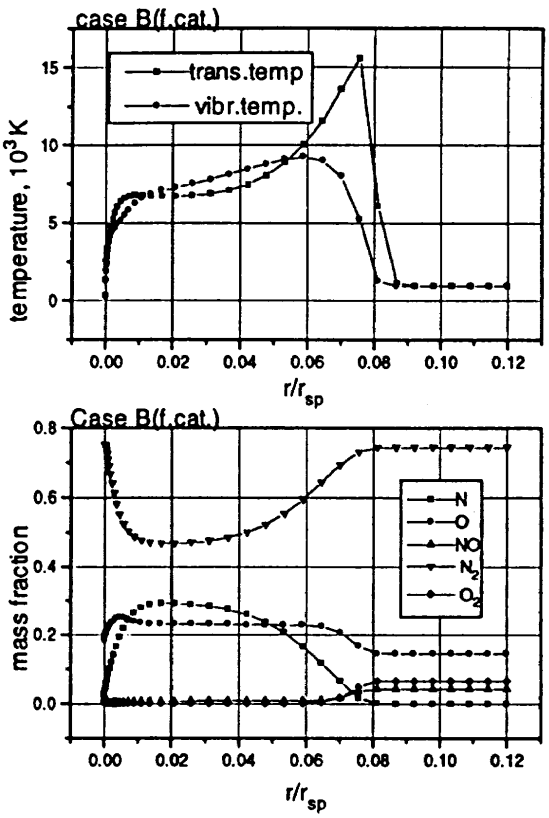

Fig.3 Case B: mass fraction and temperature along stagnation line

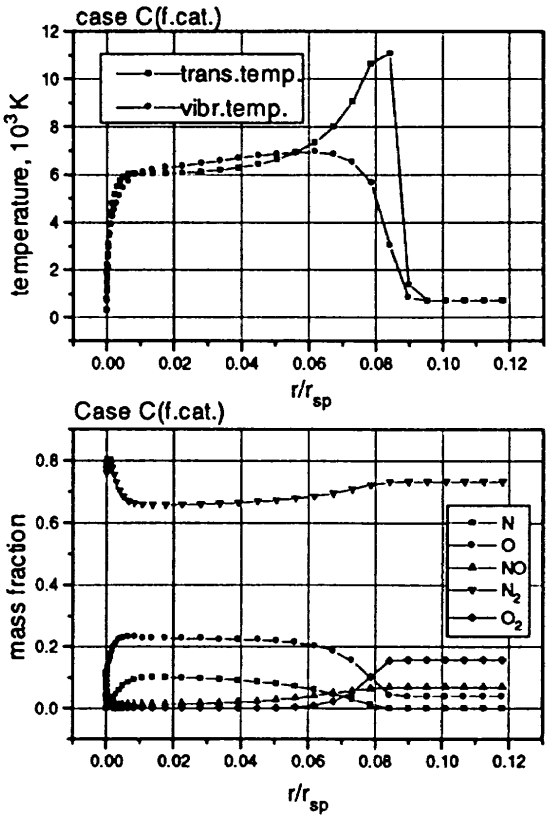

Fig.4 Case C: temperatura and mass fraction along stagnation line

Figures 2, 3, and 4 illustrate distributions of the translational/rotational and vibrational/electronic temperatures, and mass fractions of species along the stagnation streamline for the case A, B, and C, respectively, computed under the assumption that the wall surface is fully catalytic to chemical reactions. The

distance is calculated from the stagnation point and normalized with the radius of the sphere.

The translational/rotational temperature grows up abruptly at the shock wave, reaching a maximum value of approximately 15000K for the case A, 15600K for the case B, and 11100K for the case C. The vibrational/electronic mode does not change across the shock. As a result, a stretched zone is formed behind the shock where translational/rotational and vibrational/electronic modes are in non-equilibrium. Due to the relaxation process between these modes the vibrational/electronic temperature increases gradually, achieving its maximum value at the end of the relaxation process. This value is about 9200K for the cases A and B, and 7000K for the case C.

High temperature behind the shock wave initiates dissociation processes, which dissociate diatomic species (N_2, O_2, NO) and produce atomic species (N, O). This can be seen in mass fraction distributions of species (Figs.2, 3, and 4). Comparison of computed mass fractions with equilibrium composition of air under conditions obtained in the calculations show that the flow in the shock layer is mostly nonequilibrium. The equilibrium state is achieved near the wall only, where the species mass fractions tend to their freestream values due to fully catalytic boundary conditions.

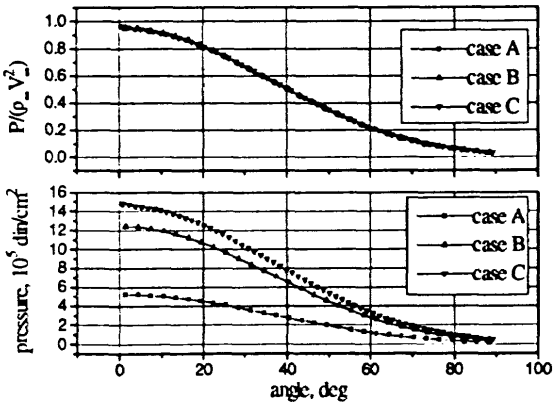

Fig.5 Pressure over sphere, f.cat. wall

The pressure distribution over the sphere surface is shown in Fig.5 for absolute values (lower graph) and normalized values (upper graph) for the case of fully catalytic case. One can see that the pressure normalized with the freestream density and velocity are in fact described by a unique curve for all cases. That is, this means a good correlation with the Newton-Busemann asymptotic theory.

The calculations with non-catalytic boundary conditions on the wall show no essential distinctions in comparison with fully catalytic wall cases in all flow parameters except for species mass fractions. Their distributions along the stagnation streamline are presented in Fig.6 for the cases A, B, and C.

The heat flux at the sphere surface with its contribution parts in translational/rotational, vibrational/electronic, and diffusion modes are shown in Figs. 7, 8, and 9 for the cases A, B, and C, respectively, for both fully catalytic and non-catalytic wall calculations. Here, we also give the experimental data obtained by the KHI (Ref.4).

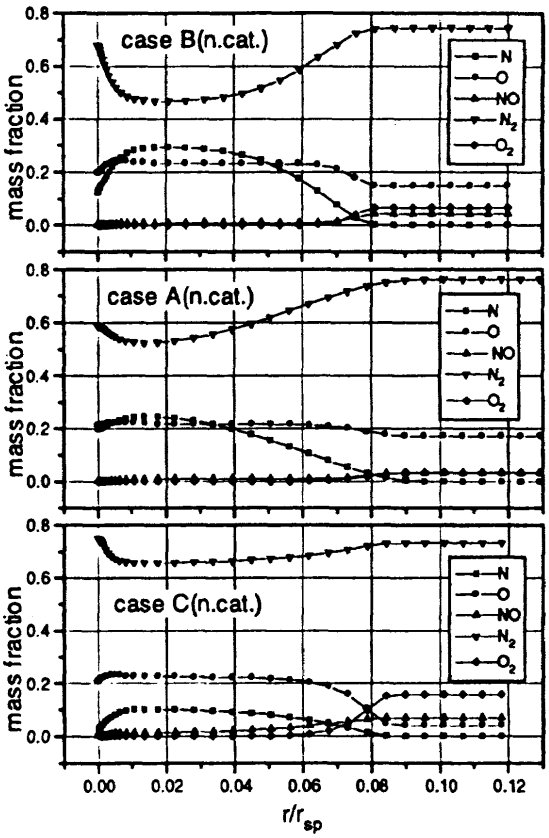

Fig.6 Non-catalytic wall: species mass fractions along the stagnation streamline

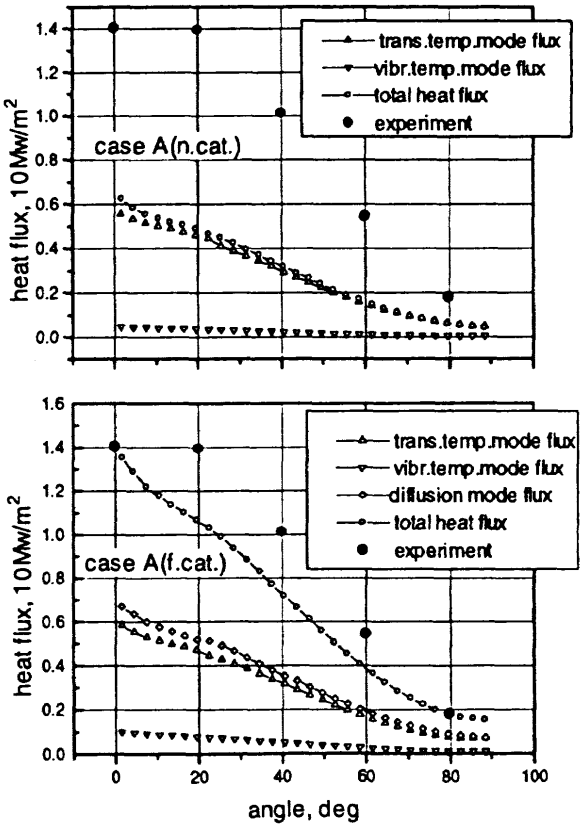

Fig.7 Case A: heat transfer rate at the wall

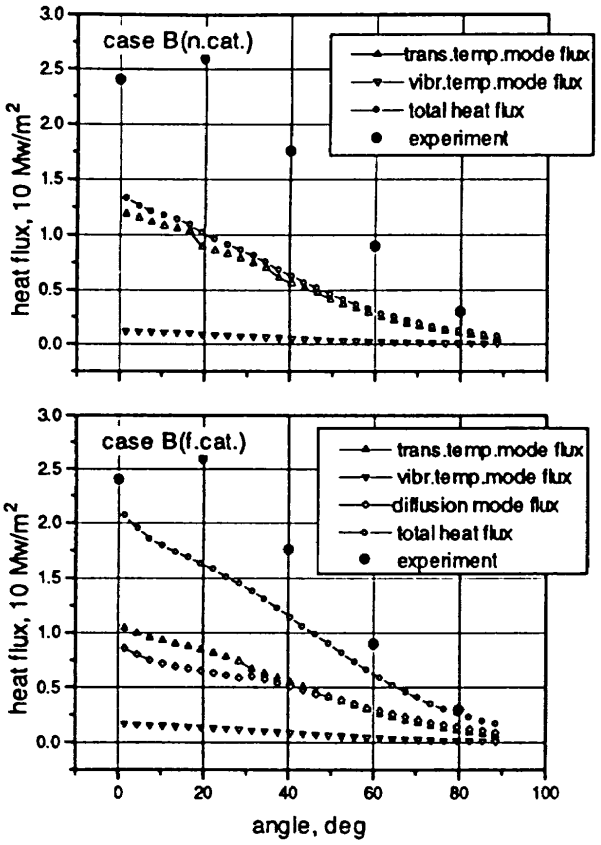

Fig.8 Case B: heat transfer rate at the wall

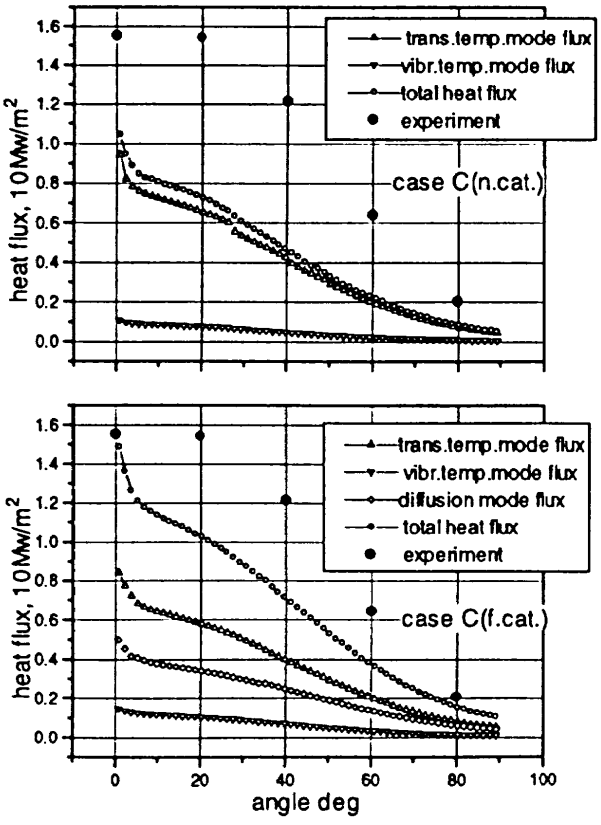

Fig.9 Case C: heat transfer rate at the wall

Main conclusions, which can be derived from the analysis of heat flux data, are made in the following. The contribution due to the convective flux in the vibrational/electronic mode is found to be considerably less that that in the translational/rotational and diffusion mode, and hence, the estimation of the corresponding dissipative coefficients seems to be of crucial importance in the prediction of heating characteristics. The heat fluxes obtained in calculations under non-catalytic wall boundary conditions are much deviated from the experimental data than those with fully catalytic wall surfaces. The latter differs from the experimental data within 20% for the cases A, and C and 40% for the case B. Especially for the case B, where even a non-monotonic profile of the heat flux over the sphere surface was observed (Fig.8), the maximum distinction in numerical and experimental data lies in a middle region, which corresponds to the angle between 20 and 40 degree. The reason for this is not clear now, but a hypothesis can be put forward that the transition to turbulent flow might happen in the boundary layer around here, leading to an increase of heat flux.

4. Blunt cone model calculations

A 140° blunt cone model with a cylindrical afterbody part (sting) utilized in many high enthalpy tunnel experiments (Refs.3, 21) is employed in the calculations described herein. The model consists of a) the forebody part I-II (Fig.10) in the form of a 140° spherically blunted cone with a base radius R_b of 7.62cm, and a nose radius R_n of 3.81cm, b) the back side of the forebody (the afterbody) II-III , and c) the cylindrical support (the sting) III-IV with a length L = 22.1cm and a diameter D = 1.91cm.

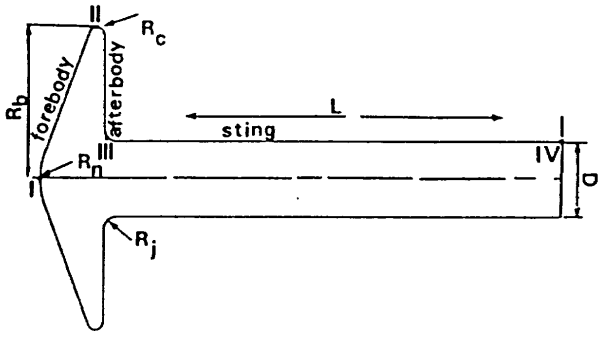

Fig.10 Geometry of blunt cone model

The forebody and the afterbody are smoothly joined by a circumference with a radius R_c of 0.382cm. The sting is connected with the afterbody through a junction radius R_j of 0.635cm.

The calculations have been performed for the freestream conditions listed below:

pressure:	$p_\infty = 5785.2 \mathrm{dyn/cm^2}$
density:	$\rho_\infty = 4.085*10^{-6} \mathrm{g/cm^3}$
velocity:	$v_\infty = 4.5395*10^5 \mathrm{cm/s}$
temperature:	$T_\infty = 489.89 \mathrm{K}$
Mach number:	$M_\infty = 10.19$
Reynolds number:	$Re_\infty = 3.79*10^5$

where the Reynolds number is based on the base diameter $2R_b$.

These parameters correspond to the test No132 in a series of high enthalpy flow experiments recently carried out at the HEG of the DLR (Ref.2), where the heat transfer rate along the blunt cone model was measured with fast response surface thermocouples on the forebody and sensitive thin film heat transfer gauges on the sting. The test No132 was implemented with a special system designed by NASA for high spatial resolution of the heat transfer on the model surface, where the model was instrumented with 113 sensors mostly located on the sting.

Air in the freestream is considered to consist of oxygen and nitrogen with the molar concentrations of 0.21 and 0.79, respectively.

The calculations are carried out with a non-uniform grid greatly clustered in the boundary layer. The grid consists of 65 cells in the direction away from the body and 160 cells in the direction along the model surface. The wall cell Reynolds number defined as $Re_{cell} = Re\,\Delta h_w / R_b$, where Δh_w is the normal spacing at the wall, is equal to 2.37 . It is expected that this is sufficient to achieve grid convergence at least in terms of heat flux distribution (Ref. 17).

At the wall surface, the vibrational/electronic temperature is assumed to be equal to the given wall temperature of 295K. The wall surface is assumed to be fully catalytic to chemical reactions.

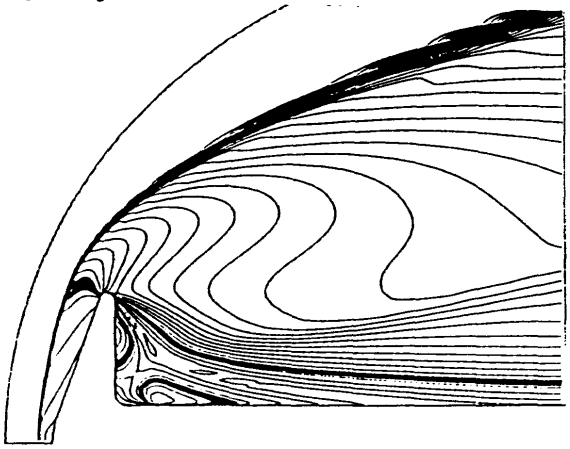

Fig.11 Mach number contours

The Mach number contours are shown in Fig.11 with a contour line increment of 0.2, where sonic lines are singled out by bold lines. It can be seen that the flow accelerates at the edge, turning toward the sting, and then separates from the wall near the edge on the afterbody. It leads to formation of a recompression shock and a zone with strong recirculation flow. The recompression shock has a small angle of about 20° with the centerline. It does not have a good resolution due to a coarse grid used in this part of the wake. Nevertheless the reattachment point and the position of the shock can be identified. The recirculation zone has a complicated structure characterized by two closed supersonic zones located on the sting and on the afterbody near the separation point.

The flow in this zone is characterized by an extensive vortex, the center of which is strongly shifted toward the separation point as shown in Fig.12 where vorticity contours are presented.

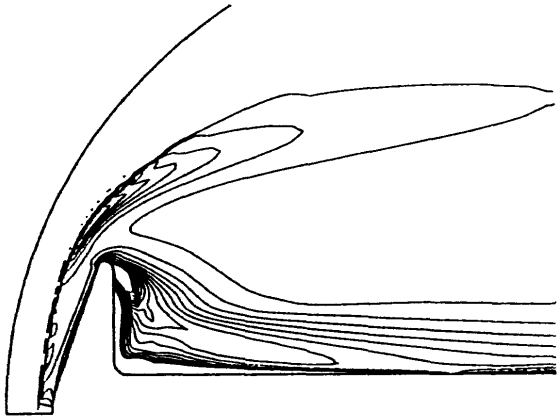

Fig.12 Vorticity contours

The following discriptions are associated with the heat transfer q_w and the pressure p_w on the model surface. The total heat transfer is calculated by the summation of 3 contribution parts: the translational temperature mode flux, the vibrational temperature mode flux, and the diffusion mode heat flux.

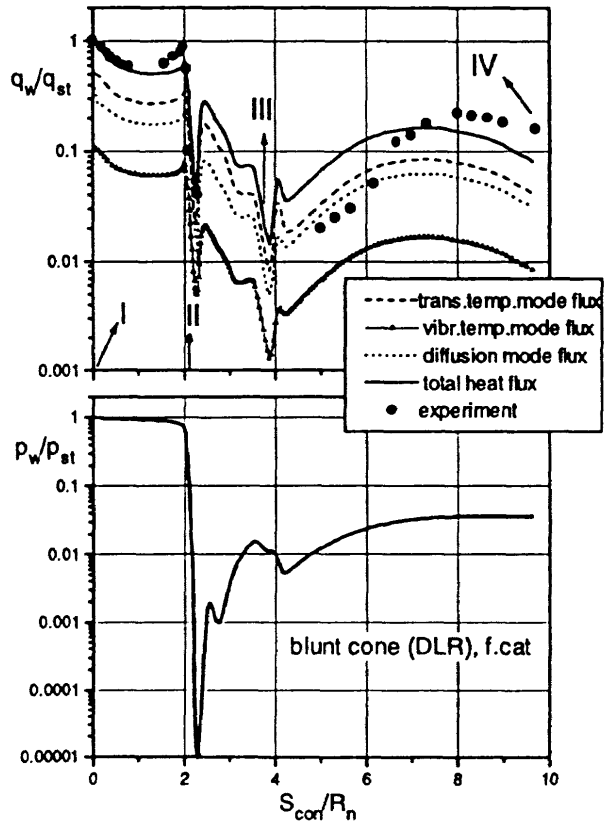

Fig.13 Normalized heat flux and pressure along the body contours

Figure 13 illustrates normalized heat flux with each contribution part and pressure along the model surface. Here, the solid symbols were obtained from the test No132 in the set of experiments performed at the HEG of the DLR (Ref.3).

The data are normalized by the stagnation point heat flux and pressure, which were found to be $q_{st} = 3.64 MW/m^2$ and $p_{st} = 8.08*10^5 din/cm^2$, respectively. The horizontal axis is the distance along the model contour S_{con} (measured from the stagnation point) normalized by the base radius R_b.

It can be seen that the numerical data are in good agreement with the experimental data except for the values near the edge of the forebody. The experiment data show a rise of heat flux at the edge up to 90% of the stagnation point value, while it is 64% in the calculations. The heat flux on the afterbody (II-III, Fig.13) abruptly drops at the edge, and suddenly rises on the upper part of the afterbody reaching the value of about 30% of the stagnation point value. This unexpected effect might be caused by the presence of a supersonic zone close to upper afterbody (Fig.11), where gas tends to come to the wall, forming a high intensity vortex around the separation point (Fig.12).

The numerical model predicts a local heat load peak on the sting (III-IV, Fig.13) caused by the compression of the flow in the shear layer with a formation of a recompression shock in the near wake. However, in comparison with the experimental data it turns out to be about 20% less, slightly shifted towards the afterbody, and spatially stretched. This might be due to a coarse grid used in this region of the wake, leading to insufficient accuracy in resolution for the recompression shock with a reattachment point.

As in the sphere calculations described above, the contribution due to the convective flux in the vibrational-electronic temperature mode is found to be considerably less than that in the translational-rotational temperature mode and the diffusion mode, which confirms that estimations of the corresponding dissipative coefficients seems to be very important in heat transfer rate predictions.

5. Summary

A numerical model for the calculation of thermochemical nonequilibrium air flows has been applied to simulate the experiments with a sphere model and a blunted cone model carried out by the KHI and the DLR, respectively. For the calculations with the blunted cone model, main features as separation of the flow, recompression shock with a reattachment point, and a recirculation zone were obtained. It was found that the recirculation zone is characterized by a vortex shifted strongly towards the separation point with two supersonic zones.

Despite good qualitative agreement with experimental data, the heat transfer obtained with the numerical model turned out to be underpredicted in comparison with the experimental data at the middle part of the sphere (20%-40%) in the sphere model calculations, and at the edge of the forebody (30% less) and in the peak value on the sting (20% less) in the blunted cone model calculations. It was also found that an abrupt heating rise on the upper part of the afterbody (blunted cone case) reaches 30% of the stagnation point value.

Acknowledgment. This work was supported in part by Grants N8Q300 and JBR100 from the ISF.

References

[1]Fay J.A., Riddel, F.R., Theory of stagnation point heat transfer in dissociated air, J. Aero. Sci., V.25, No2, 1958, pp.73-85.

[2] Anderson L.A., Effect of surface catalytic activity on stagnation heat transfer rates, AIAA J., V.11, 1973, pp.649-656.

[3]Kastell, D., Horvath, T.J., Eitelberg, G., Nonequilibrium flow expansion experiment around a blunted cone, 1995 (some conference proceeding).

[4]Kishimoto T., Hanamitsu A., Bitoh H., High enthalpy flow computation and experiment around the simple bodies, presented at High Enthalpy Flow Workshop, June 1995, NAL (Japan).

[5]Park, C., Assessment of Two-Temperature Kinetic Model for Ionizing Air, AIAA-87-1574, June 1987.

[6]Park, C., and Yoon, S., Fully Coupled Implicit Method for Thermochemical Nonequilibrium Air at Suborbital Flight Speeds, Jour. of Spacecraft, 1991, v.28, No1, pp.31-39

[7]Men'shov I.S., and Nakamura Y., An Implicit Advection Upwind Splitting Scheme for Hypersonic Air Flows in Thermochemical Nonequilibrium, in: A Collection of Technical Papers of 6th Int.Symp.on CFD, Lake Tahoe, Nevada, 1995, v.II, pp.815-821.

[8]Liou, M.-S., Steffen, C.J., A New Flux Splitting Scheme, J. Comp. Phys., 107, 1993, pp.23-39.

[9]Yoon S., Jameson A., Lower-Upper Symmetric-Gauss-Seidel Method for the Euler and Navier-Stokes Equations, AIAA Journal, 1988, v.26, No9, 1025-1026.

[10]Gnoffo, P.A., Gupta, R.N., Shinn, J.L., Conservation Equations and Physical Models for Hypersonic Air Flows in Thermal and Chemical Nonequilibrium, NASA Tech. Pap., 2867, 1989.

[11]Park, C., Nonequilibrium Hypersonic Aerothermodynamics, 1989.

[12]Lee, J.-H., Basic Governing Equations for the Flight Regimes of Aeroassisted Orbital Transfer Vehicles, Prog. Astr. Aeron., 96, 1984, pp.3-54.

[13]White, F.M., Viscous Fluid Flow, McGraw-Hill Book Comp., 1974, pp.27-36.

[14]Vincenti, W.G., Kruger, C.H., Introduction to Physical Gas Dynamics, Krieger Publ.Comp., 1993, pp.197-245.

[15]Park, C., Convergence of Computation of Chemical Reacting Flows, Prog. Astr. Aeron., 103, 1986, pp.478-513.

[16]Men'shov, I.S., Nakamura Y., Numerical Study of an Implicit AUSM with Application to Hypersonic Flows, Proc.8th Int. Conf. on CFD, Tokyo, Dec.1994, pp13-16.

[17]Men'shov, I.S., Nakamura Y., Numerical Simulation of Nonequilibrium Air Flow over Spheres, in: Proc.27th Fluid Dynamics Conf., Gifu, Japan, 1995, 169-172.

[18]Liou, M.-S., B.v Leer, Shuen, J.S., Splitting of Inviscid Fluxes for Real Gases, J.Comp.Phys., 1990, v.87, pp.1-24.

[19]Wada , Y., and Liou, M.-S., A Flux Splitting Scheme with High-Resolution and Robustnees for Discontinuities, AIAA Paper 94-0083, Jan.1994.

[20]Liou, M.-S., Progress Towards an Improved CFD Method:AUSM, AIAA Paper 95-1701, Jun.1995.

[21]Stewart, D.A., Chen, Y.K., Convective heat transfer rate distributions over a 140^0 blunt cone at hypersonic speeds in different gas environments, 1993, AIAA paper No 93-2787.

[22]Jameson, A., Yoon, S., Lower-Upper Implicit Schemes with Multiple Grids for the Euler Equations, AIAA J., 25, 7, 1987, pp.929-935.